A&A 518, L133 (2010)
DOI: 10.1051/0004-6361/201014626

Astronomy & Astrophysics
Special feature

Herschel: the first science highlights

Letter to the Editor

The β Pictoris disk imaged by *Herschel* PACS and SPIRE⋆,⋆⋆

B. Vandenbussche[1], B. Sibthorpe[2], B. Acke[1], E. Pantin[3], G. Olofsson[4], C. Waelkens[1], C. Dominik[5,6], M. J. Barlow[7], J. A. D. L. Blommaert[1], J. Bouwman[8], A. Brandeker[4], M. Cohen[9], W. De Meester[1], W. R. F. Dent[10], K. Exter[1], J. Di Francesco[11], M. Fridlund[12], W. K. Gear[13], A. M. Glauser[14,2], H. L. Gomez[13], J. S. Greaves[15], P. C. Hargrave[13], P. M. Harvey[16,17], Th. Henning[8], A. M. Heras[12], M. R. Hogerheijde[18], W. S. Holland[2], R. Huygen[1], R. J. Ivison[2,19], C. Jean[1], S. J. Leeks[20], T. L. Lim[20], R. Liseau[21], B. C. Matthews[11], D. A. Naylor[22], G. L. Pilbratt[12], E. T. Polehampton[20,22], S. Regibo[1], P. Royer[1], A. Sicilia-Aguilar[8], B. M. Swinyard[20], H. J. Walker[20], and R. Wesson[7]

(Affiliations are available in the online edition)

Received 31 March 2010 / Accepted 18 May 2010

ABSTRACT

We obtained *Herschel* PACS and SPIRE images of the thermal emission of the debris disk around the A5V star β Pic. The disk is well resolved in the PACS filters at 70, 100, and 160 μm. The surface brightness profiles between 70 and 160 μm show no significant asymmetries along the disk, and are compatible with 90% of the emission between 70 and 160 μm originating in a region closer than 200 AU to the star. Although only marginally resolving the debris disk, the maps obtained in the SPIRE 250–500 μm filters provide full-disk photometry, completing the SED over a few octaves in wavelength that had been previously inaccessible. The small far-infrared spectral index (β = 0.34) indicates that the grain size distribution in the inner disk (<200 AU) is inconsistent with a local collisional equilibrium. The size distribution is either modified by non-equilibrium effects, or exhibits a wavy pattern, caused by an under-abundance of impactors which have been removed by radiation pressure.

Key words. stars: early-type – planetary systems – circumstellar matter – stars: individual: β Pic

1. Introduction

The β Pic disk, discovered by IRAS (Aumann et al. 1984), was the first debris disk to be directly imaged in scattered light (Smith & Terrile 1984). It is seen close to edge-on and extends in the optical out to 95″, corresponding to 1800 AU (Larwood & Kalas 2001).

β Pic (A5V) is one of the closest (19.44 ± 0.05 pc, van Leeuwen 2007) and youngest debris disks. The estimated age (12 Myr, Zuckerman et al. 2001) significantly exceeds typical timescales for the survival of pristine circumstellar dust grains (e.g., Fedele et al. 2010), hence continuous replenishment of the dust, presumably through collisions of planetesimals, is needed. The closeness of the object ensures that it can also be spatially resolved at long wavelengths: Holland et al. (1998) resolved the disk at 850 μm and Liseau et al. (2003) at 1200 μm.

Optical and near-infrared observations of the inner part (<100 AU) of the disk yield evidence of asymmetries such as warps and density contrasts, which may relate to the presence of planetesimals (Kalas & Jewitt 1995; Pantin et al. 1997; Mouillet et al. 1997; Heap et al. 2000; Telesco et al. 2005). Lagrange et al. (2009) imaged a possible companion at a projected distance of 8 AU from the star.

Images of β Pic in scattered stellar light directly detect small grains and indirectly larger grains that produce the smaller ones through collisions. The grain-size distribution can be quantitatively constrained from the spectral energy distribution (SED) of the disk, in the infrared and (sub)mm domains. The spectral index of the SED at the longest wavelengths (Liseau et al. 2003; Nilsson et al. 2009) is inferred to be fairly low, which according to modeling (Draine 2006; Natta et al. 2007; Ricci et al. 2010) can be interpreted as a deficit of small grains.

In this paper, we present far-infrared imaging of the β Pic debris disk in six *Herschel* photometric bands between 70 and 500 μm. These bands cover for the first time the long-wavelength side of the peak in the thermal emission of the disk, and the large aperture of the telescope enables us to resolve the disk at far-IR wavelengths for the first time. With these data, we measure the surface brightness profiles of the disk and readdress the issue of the grain-size distribution in the inner 200 AU.

2. Observations and data reduction

We obtained maps of β Pic with the PACS and SPIRE instruments of *Herschel* (Pilbratt et al. 2010). The in-orbit performance, scientific capabilities, calibration methods, and accuracy are outlined by Poglitsch et al. (2010) for the PACS instrument and by Griffin et al. (2010) and Swinyard et al. (2010) for the SPIRE instrument. The observations were carried out during the science demonstration phase as proposed in the "Stellar Disk Evolution" guaranteed time proposal (PI G. Olofsson). Table 1 gives a summary of the observations. The deep PACS observation at 70 μm and 160 μm is a standard PACS photometer

⋆ *Herschel* is an ESA space observatory with science instruments provided by European-led Principal Investigator consortia and with important participation from NASA.

⋆⋆ Figures 2, 6, Table 1 and Appendix are only available in electronic form at http://www.aanda.org

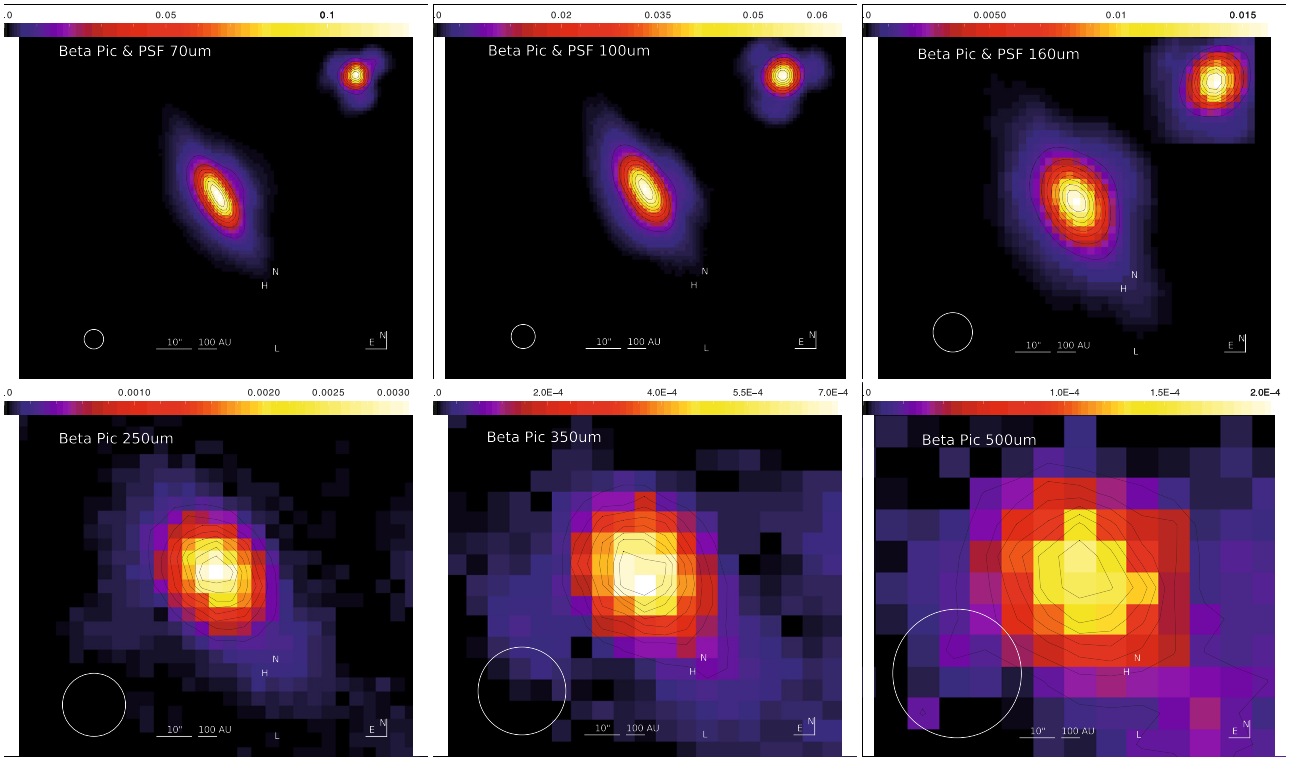

Fig. 1. Surface brightness maps of the β Pic debris disk at 70, 100, 160, 250, 350, and 500 μm. The PACS PSFs, rotated to match the position angle of the telescope at the time of the β Pic observations are depicted in the upper right corner of the images. The SPIRE PSFs are depicted in Fig. 6. All images are scaled linearly, contour lines are in steps of 10% of the peak flux. The surface brightness unit is Jy arcsec^{-2}. The white circle shows the beam $FWHM$. The position of the flux peaks observed at 850, 870, and 1200 μm by Holland et al. (1998), Nilsson et al. (2009), and Liseau et al. (2003) are indicated with H, N, and L.

scan map, split into a scan and cross-scan on the sky. The sky scan speed was 10″ s^{-1}. The homogeneously covered area of the deep map is 2.5′ × 2.5′. The observation at 100 μm is much shallower, with a single scan direction at a rate of 20″ s^{-1}, homogeneously covering an area of 2′ × 2′. The PACS beams at 70, 100, and 160 μm are 5.6, 6.8, and 11.3″ $FWHM$. In the SPIRE observation, the three bands are observed simultaneously in a standard scan map. The map coverage is 8′ × 8′. The SPIRE FWHM beam sizes in the 250, 350, and 500 μm channels are 18.1, 25.2, and 36.9″respectively.

The data processing is described in Appendix. The absolute flux calibration accuracy of the resulting PACS maps is better than 10% at 70 and 100 μm, and 20% at 160 μm (Poglitsch et al. 2010). The flux calibration accuracy of the SPIRE maps is better than 15% (Swinyard et al. 2010). The 1σ noise levels of the maps are listed in Table 2.

3. Analysis

In Fig. 1, we show the maps obtained in the three PACS filters (70, 100, and 160 μm) and the three SPIRE filters (250, 350, and 500 μm). We also compare the point spread functions (PSFs) measured on the asteroid Vesta using the same satellite scan speed, processed as the β Pic maps and rotated to align with the telescope pupil orientation on the sky during the β Pic observations as listed in online Table 1.

These images show a clearly resolved disk from 70–160 μm. Each map was fitted using a 2D Gaussian function. Within the 2″*Herschel* pointing accuracy, the Gaussian center matches the star's optical position. The fitted position angles, listed in Table 2, agree with the optical disk position angle of 30.°8 reported by Kalas & Jewitt (1995). Cross-sections orthogonal to the disk position angle in the NW to SE direction show no significant broadening compared to the PSF. The disk is not resolved in the vertical direction. The feature towards the NW, visible in the 70–160 μm images, is produced by the three-lobed PACS PSF.

Table 2. Overview of measured quantities.

λ (μm)	PA (°)	NE (″)	SW (″)	1σ noise (mJy ″$^{-2}$)	beam (″)	F_ν (Jy)
70 μm	29.°9	68	67	0.079	5.6	16.0 ± 0.8
100 μm	30.°3	55	56	0.086	8.6	9.8 ± 0.5
160 μm	28.°1	63	60	0.044	11.3	5.1 ± 0.5
250 μm		62	72	0.015	18.1	1.9 ± 0.1
350 μm		42	83	0.007	25.2	0.72 ± 0.05
500 μm		33	80	0.004	36.9	0.38 ± 0.03

Notes. Position angle PA, northeast (NE) and southwest (SW) extent (signal reaching the 1σ noise), map noise level, beam $FWHM$, and the flux density integrated over a 60″ aperture.

In Fig. 3, we present the surface brightness profiles along the disk position angle. We compare them with the cross-sections aligned in the same direction through the PSFs. At 250 and 350 μm, the disk is marginally resolved. At 500 μm, the β Pic profile shows no significant departure from the PSF profile, with the exception of a cold blob in the southwest. As can be seen in Fig. 1, the location of this feature in the 250–500 μm maps coincides with the flux peaks seen at 850 and 870 μm by Holland et al. (1998) and Nilsson et al. (2009), respectively. However, the 100 arcmin^2 region around β Pic (depicted in online Fig. 2) shows more than 50 background sources comparable to this feature in the 250 μm map. The feature is therefore probably a background source.

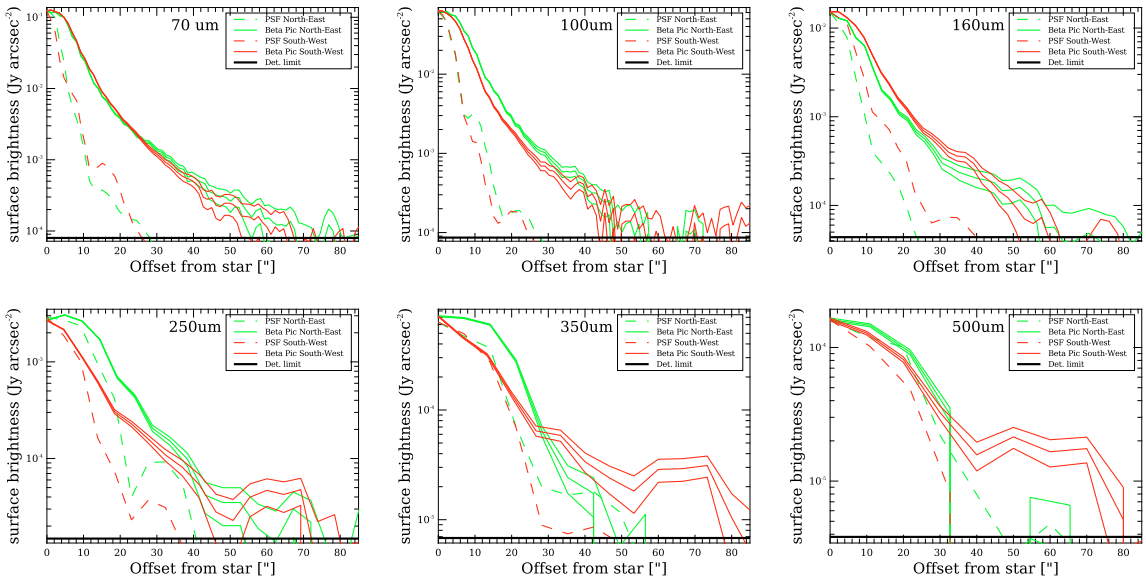

Fig. 3. Surface brightness profiles along the disk in NE-SW direction, following the 30.8° position angle. The black horizontal line shows the 1σ detection limit in the β Pic maps. The β Pic profiles are shown with the 1σ errors.

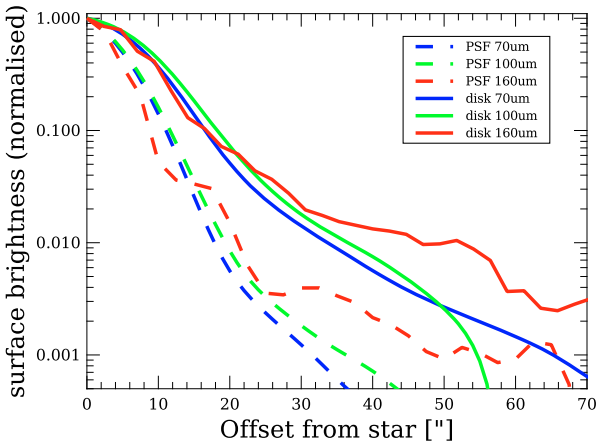

Fig. 4. Normalised surface brightness profiles along the disk in NE direction in the three PACS filters. The profiles were convolved with a Gaussian to match the spatial resolution of the 160 μm image. The same convolved profiles are shown for the PSF maps.

Other asymmetries between the northeast and southwest profile are within the errors induced by the asymmetry of the PSF. No sharp disk edge is seen; in all filters, the surface brightness declines gradually to the 1σ detection limit of the maps. Table 2 lists the extent of the detected emission region in the NE-SW direction.

The comparison of the surface brightness profiles in the three PACS filters in Fig. 4 shows the same brightness profile along the 30.8° position angle in NE direction. The 70 and 100 μm profiles were convolved with a Gaussian to match the spatial resolution at 160 μm. The same convolution was applied to the 70 and 100 μm PSF profiles. The shape of these convolved PSF profiles defers significantly from that of the 160 μm PSF profile. The wiggles in the 160 μm profile differ up to a factor of 3 from the convolved 70 and 100 μm PSF profiles. Within these uncertainties, there is no evidence of a wavelength dependent surface brightness. This indicates that the grains producing the emission at 70, 100, and 160 μm are confined to the same locus in the disk. At 70 μm, the broadening of the profile with respect to the PSF indicates that 90% of the emission originates in a region within 11″ or 200 AU of the star.

4. The far-infrared SED and grain size

We integrated the surface brightness maps over a 60″ radius circular aperture. Background subtraction was based on a rectangular region, selected close enough to the object to be within the map region with the same coverage as the center of the map. For the background outlier rejection, the DAOphot algorithm in the HIPE aperture photometry task was used. The aperture photometry obtained provides a good measure of the flux density of the integrated disk. The contribution of the stellar photosphere at these wavelengths is negligible. The error is dominated by the present uncertainties in the absolute flux calibration of both instruments. The full disk flux densities are listed in Table 2.

Figure 5 shows the new PACS and SPIRE photometry, and selected infrared and (sub-)mm flux densities from the literature. Because the disk is optically thin at these wavelengths, the wavelength dependence of the emission directly probes the dust grains, and, in particular, their size distribution. We overplot two modified Rayleigh-Jeans laws ($F_\nu \propto \nu^{(2+\beta)}$), normalized to the 160 μm datum. The spectral index β indicates the mean dust opacity $\kappa \propto \nu^\beta$. An index $\beta = 0$ corresponds to a black body with a κ independent of wavelength λ, indicating grains that are much larger than $\lambda/2\pi$. Interstellar grains, which have a size distribution $f(a) \propto a^{-q}$ with $q = 3.5$ and an upper size limit of $a_{\rm max} \sim 0.3$ μm, are characterized by $\beta = 1.8 \pm 0.2$ (Draine 2006). In protoplanetary disks, β-values from 1.5 down to 0 are found, depending on the disk geometry (Acke et al. 2004). An error-weighted least squares fit of a Rayleigh-Jeans law to the β Pic photometry at wavelengths beyond 160 μm yields $\beta = 0.34 \pm 0.07$. Nilsson et al. (2009) obtained $\beta = 0.67$ from a β-corrected black-body fit to the full disk SED, including mid-infrared photometry. The difference between both results should not be over-interpreted since both approaches are sensitive in different ways to simplifying assumptions about the temperature and size distribution within the disk. In any case, both results consistently show a value below 0.7. Ricci et al. (2010) demonstrate that such a low value cannot be explained with a $q = 3.5$ power law. This is a surprise insofar as the latter value is the expected result for a population of bodies in a standard steady-state collisional cascade (Dohnanyi 1969).

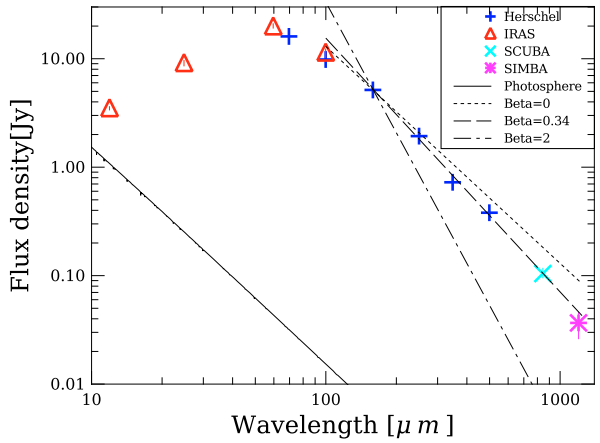

Fig. 5. The infrared to mm SED of β Pic. The PACS (70–160 μm), and the SPIRE (250–500 μm) fluxes were integrated over a 60″ radius aperture. IRAS flux densities are from the IRAS Point Source Catalog. The 850 μm SCUBA datum (Holland et al. 1998) and the 1200 μm SIMBA datum (Liseau et al. 2003) are integrated over a 40″ radius aperture. Overplotted is a Rayleigh-Jeans extrapolation of the 160 μm flux density with a spectral index $\beta = 0$ and $\beta = 2$, and the best fit to the 160–1200 μm data ($\beta = 0.34$). The stellar photosphere is a Kurucz model for $T_{\rm eff} = 9000$ K; $\log(g) = 3.9$ scaled to the 2MASS photometry $K_s = 3.52$.

The grain size distribution in β Pic must be flatter than the $q = 3.5$ power law, meaning that the fraction of small particles must be lower. Radiation pressure can push the smallest grains (with $F_{\rm rad}/F_{\rm grav} > 0.5$) onto hyperbolic orbits, hence reduce the time these particles spend in the inner part of the disk, which can decrease their volume density by two orders of magnitude (Krivov et al. 2000). The disk cannot be fully cleared of small particles, since it has been seen in scattered light out to 1800 AU. The scattering grains are probably the (sub-)μm grains that are blown out of the inner disk, where the collisions take place. However, this effect only reduces the densities for grains of size below a few micrometers, and even fully removing these grains would not change β to the observed value.

The small value of β can be interpreted in a number of ways. The grain size distribution can exhibit a wavy pattern, caused by the absence of impactors small enough to be efficiently blown out of the disk by radiation pressure. This causes an over-abundance of the grains that are just bound, which means there are more impactors for the next larger size population. The reduction of this population causes an over-abundance of a following size population and so on (Krivov et al. 2006). The wavy size distribution can lead to small values of β when measured in the FIR (Thébault & Augereau 2007). If the wavy structure were as strong as found in this paper for normal and weak material properties, it would be consistent with the small β value we have measured. However, the strength and phase of the wavy pattern in the size distribution depend on both the grain structure and the eccentricity of the dust orbits in the disk.

Alternative explanations of the small value of β cannot be excluded. There are indications that the grains produced in the deep impact experiment followed a flatter power law with $q \approx 3.1$ (Jorda et al. 2007). Laboratory experiments illustrate that fragments produced in collisions of porous aggregates can follow much flatter slopes ($q = 1.2$, Güttler et al. 2010), demonstrating that the porosity of the colliding grains should not be disregarded.

Additional dynamical models should be developed to quantify the possible contribution of these effects to the small β observed in β Pic.

5. Conclusions

We have presented images of the β Pic debris disk in six photometric bands between 70 and 500 μm using the PACS and SPIRE instruments. We resolve the disk at 70, 100, 160, and 250 μm. The images at 70–160 μm show no evidence of asymmetries in the far-infrared surface brightness along the disk of β Pic. The observed profiles are compatible with 90% of the emission originating in a region within a radius of 200 AU from the star. The disk-integrated photometry in the six *Herschel* filters provides a far infrared SED with small spectral index $\beta \approx 0.34$, which is indicative of a grain size distribution that is inconsistent with a local collisional equilibrium. The size distribution is modified by either non-equilibrium effects, or exhibits a wavy pattern, caused by the under-abundance of impactors that are small enough to be removed by radiation pressure.

Acknowledgements. PACS has been developed by a consortium of institutes led by MPE (Germany) and including UVIE (Austria); KU Leuven, CSL, IMEC (Belgium); CEA, LAM (France); MPIA (Germany); INAF-IFSI/OAA/OAP/OAT, LENS, SISSA (Italy); IAC (Spain). This development has been supported by the funding agencies BMVIT (Austria), ESA-PRODEX (Belgium), CEA/CNES (France), DLR (Germany), ASI/INAF (Italy), and CICYT/MCYT (Spain). SPIRE has been developed by a consortium of institutes led by Cardiff Univ. (UK) and including Univ. Lethbridge (Canada); NAOC (China); CEA, LAM (France); IFSI, Univ. Padua (Italy); IAC (Spain); Stockholm Observatory (Sweden); Imperial College London, RAL, UCL-MSSL, UKATC, Univ. Sussex (UK); Caltech, JPL, NHSC, Univ. Colorado (USA). This development has been supported by national funding agencies: CSA (Canada); NAOC (China); CEA, CNES, CNRS (France); ASI (Italy); MCINN (Spain); SNSB (Sweden); STFC (UK); and NASA (USA). BV acknowledges the Belgian Federal Science Policy Office via the ESA-PRODEX office. The authors thank the referee for several helpful comments.

References

Acke, B., van den Ancker, M., Dullemond, C. P., et al. 2004, A&A, 422, 621
Aumann, H. H., Beichman, C. A., Gillett, F. C., et al. 1984, ApJ, 278, L23
Dohnanyi, J. S. 1969, J. Geophys. Res., 74, 2531
Draine, B. T. 2006, ApJ, 636, 1114
Fedele, D., van den Ancker, M., Henning, T., et al. 2010, A&A, 510, A72
Griffin, M. J., Abergel, A., Abreu, A., et al. 2010, A&A, 518, L3
Güttler, C., Blum, J., Zsom, A., et al. 2010, A&A, 513, A57
Heap, S. R., Lindler, D. J., Lanz, T. M., et al. 2000, ApJ, 539, 435
Holland, W. S., Greaves, J. S., Zuckerman, B., et al. 1998, Nature, 392, 788
Jorda, L., Lamy, P., Faury, G., et al. 2007, Icarus, 187, 208
Kalas, P., & Jewitt, D. 1995, AJ, 110, 794
Krivov, A. V., Mann, I., & Krivova, N. A. 2000, A&A, 362, 1127
Krivov, A. V., Löhne, T., & Sremčević, M. 2006, A&A, 455, 509
Lagrange, A., Gratadour, D., Chauvin, G., et al. 2009, A&A, 493, L21
Larwood, J. D., & Kalas, P. G. 2001, MNRAS, 323, 402
Liseau, R., Brandeker, A., Fridlund, M., et al. 2003, A&A, 402, 183
Mouillet, D., Larwood, D., Papaloizou, B., et al. 1997, MNRAS, 292, 896
Natta, A., Testi, L., Calvet, N., et al. 2007, Protostars and Planets V, 767
Nilsson, R., Liseau, R., Brandeker, A., et al. 2009, A&A, 508, 1057
Pantin, E., Lagage, P. O., & Artymowicz, P. 1997, A&A, 327, 1123
Pilbratt, G. J., Riedinger, J. L., Passvogel, T., et al. 2010, A&A, A&A, 518, L1
Poglitsch, A., Waelkens, C., Geis, N., et al. 2010, A&A, A&A, 518, L2
Ricci, L., Testi, L., Natta, A., et al. 2010, A&A, 512, A15
Smith, B. A., & Terrile, R. J. 1984, Science, 226, 1421
Swinyard, B. M., Ade, P., Baluteau, J.-P., et al. 2010, A&A, A&A, 518, L4
Telesco, C. M., Fisher, R. S., Wyatt, M. C., et al. 2005, Nature, 433, 133
Thébault, P., & Augereau, J. 2007, A&A, 472, 169
van Leeuwen, F. 2007, A&A, 474, 653
Zuckerman, B., Song, I., Bessell, M. S., & Webb, R. A. 2001, ApJ, 562, L87

Pages 5 to 7 are available in the electronic edition of the journal at http://www.aanda.org

[1] Instituut voor Sterrenkunde, Katholieke Universiteit Leuven, Celestijnenlaan 200 D, 3001 Leuven, Belgium
e-mail: bart.vandenbussche@ster.kuleuven.be
[2] UK Astronomy Technology Centre, Royal Observatory Edinburgh, Blackford Hill, EH9 3HJ, UK
[3] Laboratoire AIM, CEA/DSM-CNRS-Université Paris Diderot, IRFU/Service d'Astrophysique, Bât.709, CEA-Saclay, 91191 Gif-sur-Yvette Cedex, France
[4] Department of Astronomy, Stockholm University, AlbaNova University Center, Roslagstullsbacken 21, 10691 Stockholm, Sweden
[5] Astronomical Institute Anton Pannekoek, University of Amsterdam, Kruislaan 403, 1098 SJ Amsterdam, The Netherlands
[6] Afdeling Sterrenkunde, Radboud Universiteit Nijmegen, Postbus 9010, 6500 GL Nijmegen, The Netherlands
[7] Department of Physics and Astronomy, University College London, Gower St, London WC1E 6BT, UK
[8] Max-Planck-Institut für Astronomie, Königstuhl 17, 69117 Heidelberg, Germany
[9] Radio Astronomy Laboratory, University of California at Berkeley, CA 94720, USA
[10] ALMA JAO, Av. El Golf 40 - Piso 18, Las Condes, Santiago, Chile
[11] National Research Council of Canada, Herzberg Institute of Astrophysics, 5071 West Saanich Road, Victoria, BC, V9E 2E7, Canada
[12] ESA Research and Science Support Department, ESTEC/SRE-S, Keplerlaan 1, 2201AZ, Noordwijk, The Netherlands
[13] School of Physics and Astronomy, Cardiff University, Queens Buildings The Parade, Cardiff CF24 3AA, UK
[14] Institute of Astronomy, ETH Zurich, 8093 Zurich, Switzerland
[15] School of Physics and Astronomy, University of St Andrews, North Haugh, St Andrews, Fife KY16 9SS, UK
[16] Department of Astronomy, University of Texas, 1 University Station C1400, Austin, TX 78712, USA
[17] CASA, University of Colorado, 389-UCB, Boulder, CO 80309, USA
[18] Leiden Observatory, Leiden University, PO Box 9513, 2300 RA, Leiden, The Netherlands
[19] Institute for Astronomy, University of Edinburgh, Blackford Hill, Edinburgh EH9 3HJ, UK
[20] Space Science and Technology Department, Rutherford Appleton Laboratory, Oxfordshire, OX11 0QX, UK
[21] Department of Radio and Space Science, Chalmers University of Technology, Onsala Space Observatory, 439 92 Onsala, Sweden
[22] Institute for Space Imaging Science, University of Lethbridge, Lethbridge, Alberta, T1J 1B1, Canada

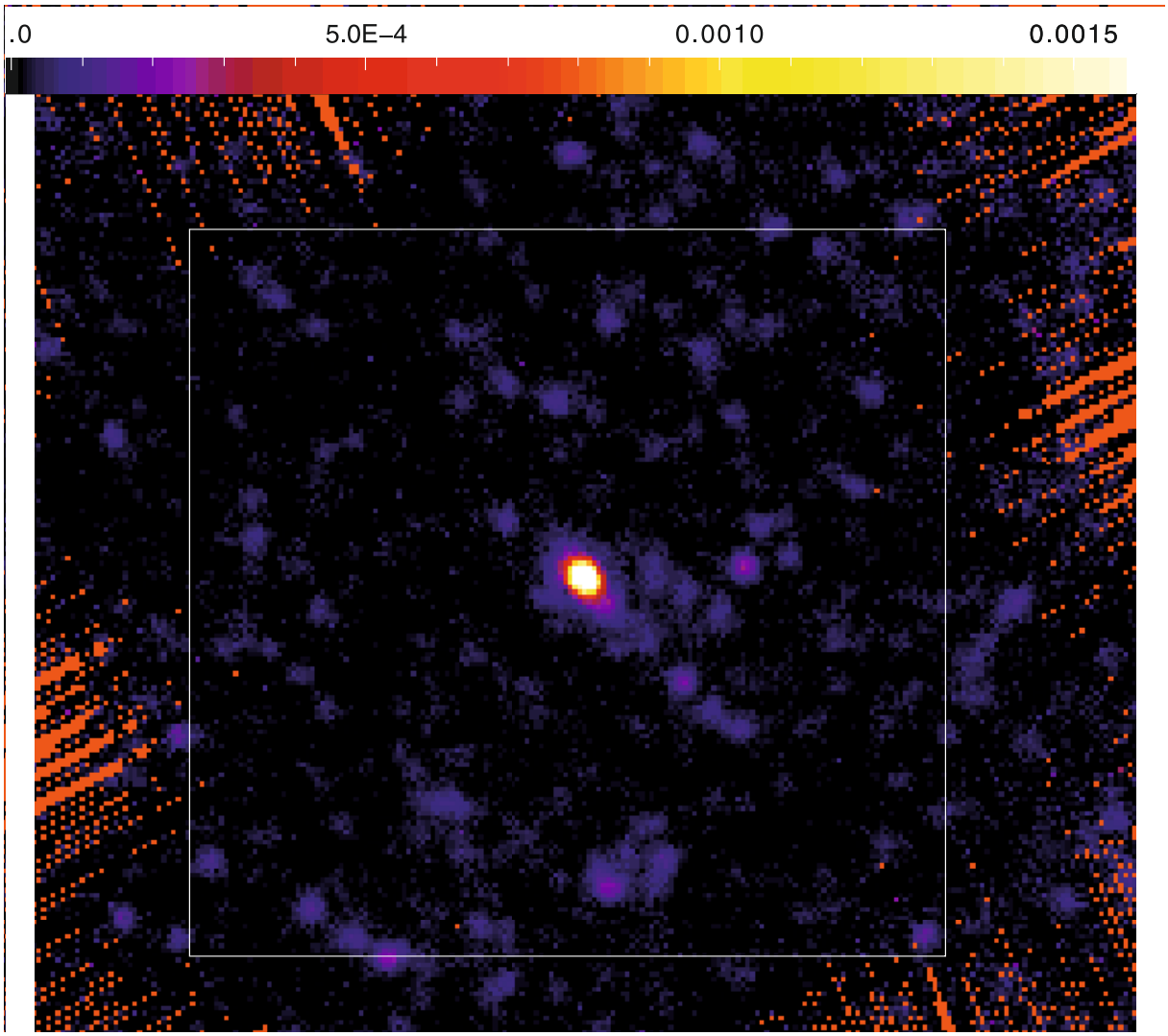

Fig. 2. The 250 μm SPIRE map around the β Pic disk. The $10 \times 10'$ region delimited by the white square shows more than 50 background sources comparable to the cold blob seen in the southwest of the disk.

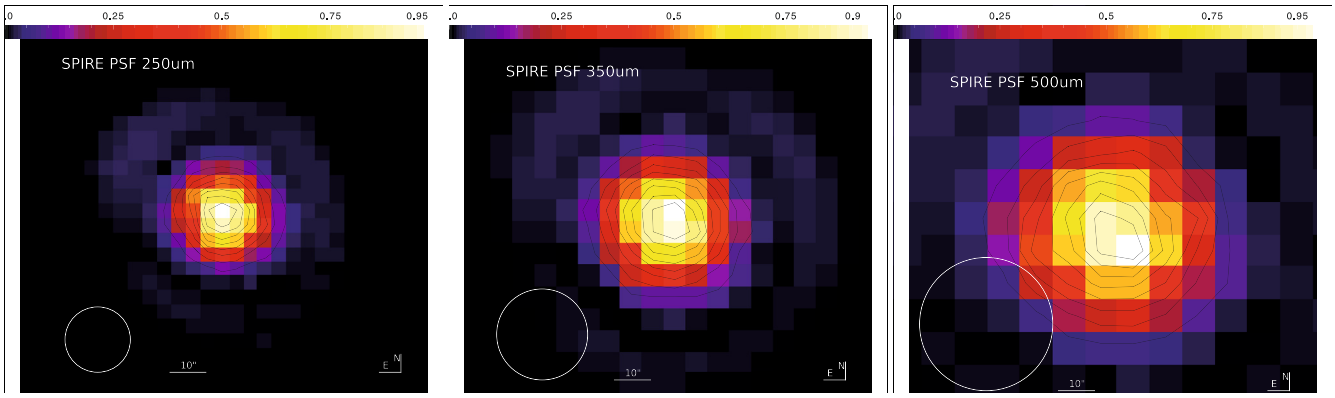

Fig. 6. The 250, 350 and 500 μm SPIRE PSFs, rotated to match the position angle at the time of the β Pic observations. The PSF images are scaled linearly, contour lines are in steps of 10% of the peak flux. The white circle shows the beam $FWHM$.

Table 1. Observation log.

	Observation	Date	Pos angle	Duration	Filters
SPIRE	1342187327	2009-11-30	154.96°	3336 s	250,350,500
PACS	1342185457	2009-10-07	106.54°	866 s	100,160
PACS	1342186613	2009-11-01	130.98°	5506 s	70, 160
PACS	1342186612	2009-11-01	130.98°	5506 s	70, 160

Appendix A: Data reduction

The PACS data were processed in the *Herschel* interactive analysis environment HIPE (v3.0), applying the standard pipeline steps. The flux conversion was done using version 5 of the response calibration. Signal glitches due to cosmic ray impacts were masked out in two steps. First the PACS photMMTDeglitching task in HIPE was applied on the detector timeline. Then a first coarse map was projected, which is then used as a reference for the second level deglitching HIPE task IIndLevelDeglitch. In the detector time series we masked the region around the source prior to applying a high-pass filter to remove the low frequency drifts. The scale of the high pass filter was taken to be half the length of an individual scan leg on the sky, i.e. 3.7′. The detector time series signals were then summed up into a map using the PACS photProject task. The pixel scale for the 70 and 100 μm maps was set to 1″, while the scale for the 160 μm map was 2″. For the deep map in the 70 and 160 μm filter we combined the two detector time series and projected these together.

The SPIRE data were also reduced using HIPE and maps were obtained via the default naiveMapper task. The SPIRE observation consists of several repetitions of a map observation of the same area. As a result it was possible to project the data with a pixel size of 4, 6, and 9″ while still maintaining complete sampling across the source.